Geomorphology 308 (2018) 161–174

Contents lists available at ScienceDirect

Geomorphology

journal homepage: www.elsevier.com/locate/geomorph

Delineation of gravel-bed clusters via factorial kriging

Fu-Chun Wu [a,*], Chi-Kuei Wang [b], Guo-Hao Huang [c]

[a] Department of Bioenvironmental Systems Engineering, National Taiwan University, Taipei, Taiwan
[b] Department of Geomatics, National Cheng Kung University, Tainan, Taiwan
[c] Geographic Information System Research Center, Feng Chia University, Taichung, Taiwan

ARTICLE INFO

Article history:
Received 22 November 2017
Received in revised form 3 February 2018
Accepted 5 February 2018
Available online 16 February 2018

Keywords:
Gravel-bed rivers
Clusters
Delineation
Factorial kriging
Digital elevation model (DEM)

ABSTRACT

Gravel-bed clusters are the most prevalent microforms that affect local flows and sediment transport. A growing consensus is that the practice of cluster delineation should be based primarily on bed topography rather than grain sizes. Here we present a novel approach for cluster delineation using patch-scale high-resolution digital elevation models (DEMs). We use a geostatistical interpolation method, i.e., factorial kriging, to decompose the short- and long-range (grain- and microform-scale) DEMs. The required parameters are determined directly from the scales of the nested variograms. The short-range DEM exhibits a flat bed topography, yet individual grains are sharply outlined, making the short-range DEM a useful aid for grain segmentation. The long-range DEM exhibits a smoother topography than the original full DEM, yet groupings of particles emerge as small-scale bedforms, making the contour percentile levels of the long-range DEM a useful tool for cluster identification. Individual clusters are delineated using the segmented grains and identified clusters via a range of contour percentile levels. Our results reveal that the density and total area of delineated clusters decrease with increasing contour percentile level, while the mean grain size of clusters and average size of anchor clast (i.e., the largest particle in a cluster) increase with the contour percentile level. These results support the interpretation that larger particles group as clusters and protrude higher above the bed than other smaller grains. A striking feature of the delineated clusters is that anchor clasts are invariably greater than the D_{90} of the grain sizes even though a threshold anchor size was not adopted herein. The average areal fractal dimensions (Hausdorff-Besicovich dimensions of the projected areas) of individual clusters, however, demonstrate that clusters delineated with different contour percentile levels exhibit similar planform morphologies. Comparisons with a compilation of existing field data show consistency with the cluster properties documented in a wide variety of settings. This study thus points toward a promising, alternative DEM-based approach to characterizing sediment structures in gravel-bed rivers.

1. Introduction

Gravel-bed rivers exhibit a wide variety of bedforms ranging in scale from microforms (e.g., imbrication, cluster), mesoforms (e.g., transverse rib, stone cell, step-pool, pool-riffle), macroforms (e.g., bar), to megaforms (e.g., floodplain, terraces) (Hassan et al., 2008). Among these, clusters are the most prevalent microforms, observed to cover 10–50% of the bed surface (Wittenberg, 2002; Papanicolaou et al., 2012). Clusters have drawn much attention from river scientists and engineers due to their impacts on: (1) local turbulence structures (Buffin-Bélanger and Roy, 1998; Lawless and Robert, 2001a; Lacey and Roy, 2007; Strom et al., 2007; Hardy et al., 2009; Curran and Tan, 2014a; Rice et al., 2014), (2) flow resistance (Hassan and Reid, 1990; Clifford et al., 1992; Lawless and Robert, 2001b; Smart et al., 2002), (3) sediment transport (Brayshaw et al., 1983; Brayshaw, 1984, 1985; Billi, 1988; Paola and Seal, 1995; Hassan and Church, 2000; Strom et al., 2004), and (4) bed stability (Reid et al., 1992; Wittenberg and Newson, 2005; Oldmeadow and Church, 2006; Mao, 2012). Besides, clusters also provide insights into the flow and sediment supply conditions of their formation (Papanicolaou et al., 2003; Wittenberg and Newson, 2005; Strom and Papanicolaou, 2009; Mao et al., 2011).

The term "clusters" was traditionally used by many researchers to refer to the so-called "pebble clusters", which normally comprise three components: obstacle, stoss, and wake (Brayshaw, 1984). The obstacle is a large clast providing an anchor for cluster formation; upstream of the obstacle is an accumulation of smaller particles that constitute the stoss zone; downstream of the obstacle is a wake zone characterized by deposition of fine material. More recently, clusters have been perceived more broadly to refer to "*discrete, organized groupings of larger particles that protrude above the local mean bed level*" (Strom and Papanicolaou, 2008; Curran and Tan, 2014a). Using this broad working definition, researchers have identified cluster microforms with a variety of shapes, such as rhombic clusters, complex

* Corresponding author.
E-mail address: fcwu@ntu.edu.tw (F.-C. Wu).

https://doi.org/10.1016/j.geomorph.2018.02.013

clusters, line clusters, comet clusters, ring clusters, heap clusters, triangle clusters, and diamond clusters (e.g., de Jong and Ergenzinger, 1995; Wittenberg, 2002; Strom and Papanicolaou, 2008; Hendrick et al., 2010). Papanicolaou et al. (2012) used the areal fractal (Hausdorff-Besicovich) dimensions of the projected areas to discriminate the planform morphologies of the clusters.

Although the broad definition of clusters has opened up new avenues for recent progress in cluster research, to date identification of clusters still relies largely on visual inspection (e.g., Entwistle et al. 2008; Strom and Papanicolaou, 2008; Hendrick et al., 2010; L'Amoreaux and Gibson, 2013). A set of predetermined criteria for cluster identification are normally adopted in these studies. A typical example is given here: (1) A cluster consists of a minimum number of (e.g., 3 or 4) abutting or imbricated particles; (2) at least one of these particles is an anchor clast greater than the specified grain size (e.g., D_{50} or D_{84}) of the bed surface; (3) a cluster protrudes above the surrounding bed surface (e.g., Oldmeadow and Church, 2006; Hendrick et al., 2010). As can be seen, specifying a minimum number of constituent particles and a threshold grain size for anchor clast is somewhat arbitrary and based on the rule of thumb. The subjectivity of the "gestalt sampling" could produce operational bias. In particular, researchers have found it extremely difficult to visually recognize bed structures whose dimensions are of the same order of magnitude as their spacing and the grain sizes of their constituent particles (Entwistle et al. 2008; L'Amoreaux and Gibson, 2013).

In laboratory settings, identification of clusters was recently advanced by a combined analysis of bed-surface images and digital elevation models (DEMs) (Curran and Tan, 2014a; Curran and Waters, 2014), with the procedure described as follows. First, clusters are visually identified by the particle arrangements shown in the digital photos. Then, the visually identified clusters are verified with the DEM, checking whether clusters are discrete and protruding above the mean bed level by a specified minimum height (e.g., D_{85} or D_{95}). Last, each verified cluster is confirmed by checking whether the cluster consists of a recognizable anchor clast $>D_{90}$, around which at least two particles $>D_{50}$ were deposited. In contrast to the previous laboratory approaches that used only images or DEMs to identify clusters (Mao, 2012; Piedra et al., 2012; Heays et al., 2014), the combined use of images and DEMs represents technological progress, providing a more robust approach. This approach, however, continues to rely on visual inspection at the identification stage and specification of some quantitative criteria (e.g., threshold protrusion height and grain sizes) at the verification and confirmation stages, thus is prone to a certain degree of subjective judgment.

Attempts to apply advanced methods to studies of field clusters have been made by two groups of researchers. The first group (Entwistle et al. 2008) used the DEM derived from terrestrial laser scanning (TLS) and an optimized moving window to compute the local standard deviations (SD) of bed elevation across a study reach. The resultant SD surface was interrogated to extract the SD that corresponded to the observed clusters. The statistics derived from the classified SD were then applied to a validation DEM to produce a map of predicted clusters. The density and spacing metrics of these predicted clusters were consistent with field observations, while the shapes and constituent grains of individual clusters were not resolvable with this statistical approach. By contrast, the second group (L'Amoreaux and Gibson, 2013) used image analysis and nearest neighbor statistics to quantify the relative abundance and spatial scale of clusters, yet individual clusters were not resolvable with such spatial statistics. The most debatable aspect of this approach is, perhaps, to collectively treat large grains ($>D_{84}$) and medium grains (between D_{50} and D_{84}) as clusters just because they were found in proximity to similar grains more frequently than the spatially random null hypothesis would predict. The lack of a topographic component in this type of analysis, however, made clusters a 2D statistical feature of plane sampling rather than a 3D morphological feature of bed structures.

While the use of DEMs in cluster identification has proved promising in laboratory settings, extending this approach to field studies would require: (1) high-resolution DEMs that resolve both the grain- and microform-scale topographies, and (2) DEM-based delineation of clusters. High-resolution DEMs that capture grain-scale details over the reach-scale extent are now achievable using the hyperscale survey methods, such as TLS or Structure-from-Motion photogrammetry (see reviews by Milan and Heritage (2012) and Brasington et al. (2012)). However, a standardized DEM-based method for delineating clusters is still lacking. Here we present a novel, DEM-based approach for cluster delineation. This approach is facilitated by the feature recognition capability of the factorial kriging that decomposes the grain- and microform-scale components of DEM. The grain-scale DEM serves as an aid for segmentation of grain boundaries, while the microform-scale DEM is used to identify individual clusters. The delineated clusters are compared with a compilation of existing field data to confirm the robustness of the presented approach.

2. Factorial kriging

The DEM of a gravel-bed surface may be considered as a random field of spatial elevation data (e.g., Matheron, 1971; Journel and Huijbregts, 1978; Furbish, 1987; Robert, 1988; Goovaerts, 1997; Nikora et al., 1998), where the dependency between the bed elevations at two locations is expressed as a function of the spatial lag, i.e., the separation distance and direction between the two locations. The organization of the gravel-bed surface has been investigated by many researchers using the semivariogram (or simply called variogram) (e.g., Robert, 1988, 1991; Nikora et al., 1998; Butler et al., 2001; Marion et al., 2003; Aberle and Nikora, 2006; Cooper and Tait, 2009; Hodge et al., 2009; Mao et al., 2011; Huang and Wang, 2012; Curran and Waters, 2014), which is a second-order structure function summarizing all the information about the spatial variation in bed elevation over a range of scales. The empirical (also termed sample or experimental) 2D variogram of the DEM, denoted as $\hat{\gamma}(\mathbf{h})$, may be expressed by a general form of semivariance as follows:

$$\hat{\gamma}(\mathbf{h}) = \frac{1}{2N(\mathbf{h})} \sum_{i=1}^{N(\mathbf{h})} [z(\mathbf{x}_i) - z(\mathbf{x}_i + \mathbf{h})]^2 \tag{1}$$

where $\mathbf{h}=$ lag vector separating locations $\mathbf{x}_i$ and $\mathbf{x}_i + \mathbf{h}$; $z(\mathbf{x})=$ bed elevation at $\mathbf{x}$; $N(\mathbf{h})$=number of data pairs separated by $\mathbf{h}$, typically $\mathbf{h}$ is limited to half of the DEM extent to ensure that sufficient data pairs are used. Use of Eq. (1) also requires that bed elevations are normally distributed and second-order stationary (Butler et al., 2001; Hodge et al., 2009). Hence, the elevation data must be normalized to a zero mean and detrended with a trend surface to remove first-order nonstationarity (Oliver and Webster, 1986; Hodge et al., 2009). The detrended (or residual) elevations retain the topographies of sediment grains and microforms, with the general bed slope removed.

Eq. (1) may be used to calculate the semivariance $\hat{\gamma}(\mathbf{h})$ over a range of $\mathbf{h}$, resulting in an empirical variogram surface that shows the spatial variability of bed elevation at different scales and along different directions. The variogram may be also plotted as a 1-D profile along a specific direction of interest. Such a 1-D directional variogram has been used extensively to investigate the multiscale properties of the gravel-bed surface (Robert, 1988; Nikora et al., 1998; Butler et al., 2001; Hodge et al., 2009; Huang and Wang, 2012). Depending on the resolution and extent of the DEM, and whether bedforms are present, the variogram profile may exhibit single or multiple scaling regions that correspond to different scales of the bed structures. Fig. 1 demonstrates a schematic empirical variogram profile (solid circles) that exhibits two scaling regions. The first region, with the lags ranging between $[0, a_1]$, corresponds to the grain-scale structure. The second region, with the lags ranging between $[a_1, a_2]$, corresponds to the microform-scale structure. At lags greater than a_2, the semivariance remains a constant sill value, which corresponds to a saturation region where the spatial

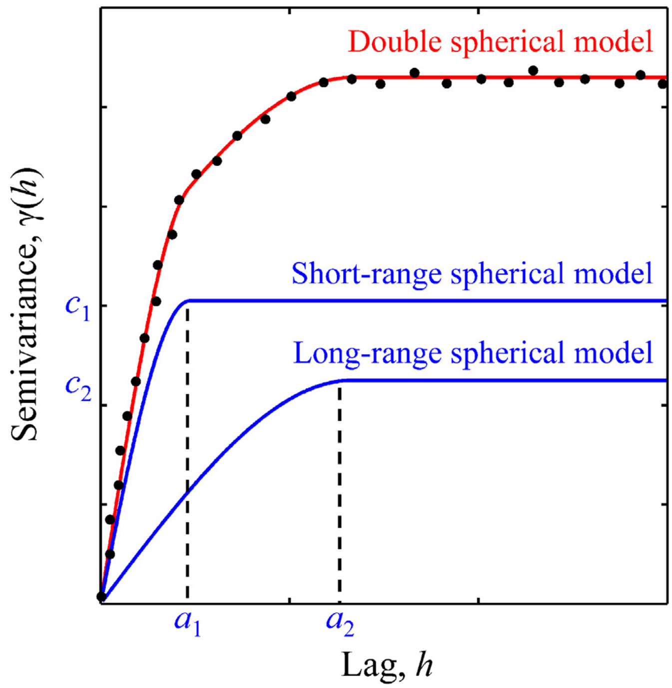

Fig. 1. A schematic empirical variogram profile (solid circles) that exhibits two scaling regions. Lags between [0, a_1] correspond to grain-scale structure; lags between [a_1,a_2] correspond to microform-scale structure; lags $>a_2$ correspond to saturation region with constant sill. The empirical variogram profile is fitted with a double spherical model (red line) that combines linearly two single spherical models (blue lines), one has a short range a_1, the other has a long range a_2, with c_1 and c_2 being the corresponding sills.

dependency is minimal and no longer varies with the lag. The variogram profile may exhibit more than two scaling regions if bedforms at larger scales (e.g., mesoform or macroform) are also present. On the contrary, the variogram profile may not reach a constant sill if the extent of the DEM is not large enough or bed elevations are not completely stationary (Hodge et al., 2009; Huang and Wang, 2012). It should be noted here that to capture the mean scales of sediment grains and microforms in all directions, an omni-directional variogram profile integrating all directional variograms was used in this study, following the suggestion of Isaaks and Srivastava (1989).

To be useful in the kriging, the empirical variogram profile is fitted with a continuous, basic mathematical model. For a variogram profile that exhibits multiple scales, a nested model (i.e., a linear combination of basic mathematical models) may be used to describe the multiscale bed structure. For example, linear, exponential, and spherical models are among the most frequently used basic mathematical models (Atkinson, 2004; Webster and Oliver, 2007). For the schematic diagram shown in Fig. 1, the empirical variogram is fitted with a double spherical model (red line), which is a nested model that combines linearly two spherical models (blue lines), one with a short range a_1 and the other with a long range a_2, which may be expressed as follows (Webster and Oliver, 2007):

$$\gamma(h)=\gamma^1(h)+\gamma^2(h)$$
$$=\begin{cases} \underbrace{c_1\left[\dfrac{3h}{2a_1}-\dfrac{1}{2}\left(\dfrac{h}{a_1}\right)^3\right]}_{\gamma^1(h)}+\underbrace{c_2\left[\dfrac{3h}{2a_2}-\dfrac{1}{2}\left(\dfrac{h}{a_2}\right)^3\right]}_{\gamma^2(h)} & \text{for } 0<h\le a_1 \\ \underbrace{c_1}_{\gamma^1(h)}+\underbrace{c_2\left[\dfrac{3h}{2a_2}-\dfrac{1}{2}\left(\dfrac{h}{a_2}\right)^3\right]}_{\gamma^2(h)} & \text{for } a_1<h\le a_2 \\ \underbrace{c_1}_{\gamma^1(h)}+\underbrace{c_2}_{\gamma^2(h)} & \text{for } h>a_2 \end{cases} \tag{2}$$

where $\gamma(h)=$ theoretical variogram model, to be differentiated from the empirical variogram $\hat{\gamma}(h)$ given in Eq. (1), here $h=|\mathbf{h}|$ is omni-directional lag; $\gamma^1(h)$ and $\gamma^2(h)$ are short- and long-range variograms; (a_1,c_1) and (a_2,c_2) are, respectively, the pairs of (range, sill) of $\gamma^1(h)$ and $\gamma^2(h)$, evaluated using, e.g., the gstat package of the open source software R (Pebesma, 2004). In this study, the range values a_1 and a_2 correspond to the grain and microform scales, respectively. Once $\gamma(h)$ is decomposed into $\gamma^1(h)$ and $\gamma^2(h)$, they can be used in the factorial kriging, described as follows.

Factorial kriging (FK) is a geostatistical interpolation method devised by Matheron (1982) that allows the decomposed components of a regionalized variable to be individually estimated and mapped. FK has been widely applied in a variety of research fields, e.g., image processing and analysis for remote sensing (Wen and Sinding-Larsen, 1997; Oliver et al., 2000; Van Meirvenne and Goovaerts, 2002; Goovaerts et al., 2005a; Ma et al., 2014), water and soil environmental monitoring (Goovaerts et al., 1993; Goovaerts and Webster, 1994; Dobermann et al., 1997; Bocchi et al., 2000; Castrignanò et al., 2000; Alary and Demougeot-Renard, 2010; Allaire et al., 2012; Lv et al., 2013; Bourennane et al., 2017), geophysics and geochemistry exploration (Galli et al., 1984; Sandjivy, 1984; Jaquet, 1989; Yao et al., 1999; Dubrule, 2003; Reis et al., 2004), risk assessment and crime management (Goovaerts et al., 2005b; Kerry et al., 2010), among many others. Despite its extensive application, to date FK has not been applied to the delineation of cluster microforms.

The theory of FK can be found in textbooks dedicated to geostatistics (e.g., Goovaerts, 1997; Webster and Oliver, 2007), thus it is only briefly summarized here. Kriging generally refers to geostatistical predictions that estimate the value at any point using a set of nearby sample values. Consider the bed elevation as a spatial random variable $Z(\mathbf{x})$, the kriged estimate of Z at a point $\mathbf{x}_0$, denoted as $\hat{Z}(\mathbf{x}_0)$, is a weighted average of N available data, $z(\mathbf{x}_1)$, $z(\mathbf{x}_2)$, …, $z(\mathbf{x}_N)$, expressed by

$$\hat{Z}(\mathbf{x}_0)=\sum_{i=1}^{N}\lambda_i z(\mathbf{x}_i) \tag{3}$$

where λ_i are weighting factors to be determined. The weighting factors must sum to unity to ensure an unbiased estimate, and the estimation variance is minimized subject to the non-bias condition. These two constraints lead to the following system of ordinary kriging (OK) equations:

$$\sum_{i=1}^{N}\lambda_i=1 \tag{4a}$$

$$\sum_{j=1}^{N}\lambda_j\gamma(\mathbf{x}_i,\mathbf{x}_j)+\psi(\mathbf{x}_0)=\gamma(\mathbf{x}_i,\mathbf{x}_0) \quad \text{for} \quad i=1,2,\ \ldots,N \tag{4b}$$

where $\gamma(\mathbf{x}_i,\mathbf{x}_j)=$ semivariance of Z between $\mathbf{x}_i$ and $\mathbf{x}_j$, for omni-directional variograms $\gamma(h)$ is used, $h=|\mathbf{x}_i-\mathbf{x}_j|$; $\psi(\mathbf{x}_0)=$ Lagrange multiplier, introduced to achieve variance minimization. For the system given in Eqs. (4a) and (4b), $N+1$ equations are used to solve $N+1$ unknowns λ_1, λ_2, …, λ_N and $\psi(\mathbf{x}_0)$. The solved weighting factors are used in Eq. (3) for an "ordinary kriged" estimate of Z. To estimate the individual components of Z at different scales, however, FK will be used as follows.

For a variogram exhibiting two scaling regions (Fig. 1), i.e., short- and long-range (or grain- and microform-scale) structures (Robert, 1988; Huang and Wang, 2012), the residual elevation $Z(\mathbf{x})$ may be expressed as a sum of two elevation components:

$$Z(\mathbf{x})=Z^1(\mathbf{x})+Z^2(\mathbf{x}) \tag{5}$$

where $Z^k(\mathbf{x})=$ k-th component, $k=1$ and 2 denotes short- and long-range components, respectively. Assuming that the two components are uncorrelated, the omni-directional variogram of Z, $\gamma(h)$, is a nested combination of short- and long-range omni-directional variograms $\gamma^1(h)$ and $\gamma^2(h)$, as shown in Eq. (2). Similar to the ordinary kriging in Eq. (3), each elevation component Z^k may be estimated with a weighted average of available data $z(\mathbf{x}_i)$ by the factorial kriging:

$$\hat{Z}^k(\mathbf{x}_0) = \sum_{i=1}^{N} \lambda_i^k z(\mathbf{x}_i) \quad \text{for } k = 1, 2 \tag{6}$$

where $\hat{Z}^k$ = factorial kriged estimate of Z^k, and λ_i^k are weighting factors for the k-th component. The weighting factors are determined by solving the following system of FK equations:

$$\sum_{i=1}^{N} \lambda_i^k = 0 \tag{7a}$$

$$\sum_{j=1}^{N} \lambda_j^k \gamma(\mathbf{x}_i, \mathbf{x}_j) - \psi^k(\mathbf{x}_0) = \gamma^k(\mathbf{x}_i, \mathbf{x}_0) \quad \text{for } i = 1, 2, \ldots, N \tag{7b}$$

where $\psi^k(\mathbf{x}_0)$= Lagrange multiplier; here $\gamma^k(\mathbf{x}_i,\mathbf{x}_0)$ for $k = 1$ and 2 are, respectively, replaced by $\gamma^1(h)$ and $\gamma^2(h)$ determined from Eq. (2), and $\gamma(\mathbf{x}_i,\mathbf{x}_j)$ is replaced by $\gamma(h)$. Eq. (7a) states that λ_i^k must sum to 0 over i (rather than 1) to ensure an unbiased estimate and accord with Eq. (5), while Eq. (7b) states that λ_i^k are selected to reach a minimum estimation variance. The system in Eqs. (7a) and (7b) is solved for each scale (each k) to determine the weighting factors λ_i^k, which are used in Eq. (6) to estimate individual components of spatial elevations, referred to as "factorial kriged (FK) DEM components".

As an illustration, we present in Fig. 2 a gravel-bed patch collected from Nanshih Creek (Taiwan) to show the ordinary kriged (OK) DEM and the short- and long-range components of the factorial kriged (FK) DEM. It is evident that the full bed topography (Fig. 2A) is the superposition of grain- and microform-scale topographies (Fig. 2B and C). The short-range FK DEM exhibits a flat bed, with 90% of the elevations in a narrow range between −0.04 and +0.03 m (Fig. 2D). The long-range FK DEM is smoother than the OK DEM, with 90% of the elevations in a range between −0.12 and +0.09 m, slightly smaller than the 90% elevation range of the OK DEM (between −0.14 and +0.1 m). Individual grains are sharply outlined in the short-range FK DEM, suggesting that the grain-scale DEM may well serve as an aid for segmentation of grain boundaries. Individual grains are not fully recognizable in the long-range FK DEM, while groupings of particles emerge as small-

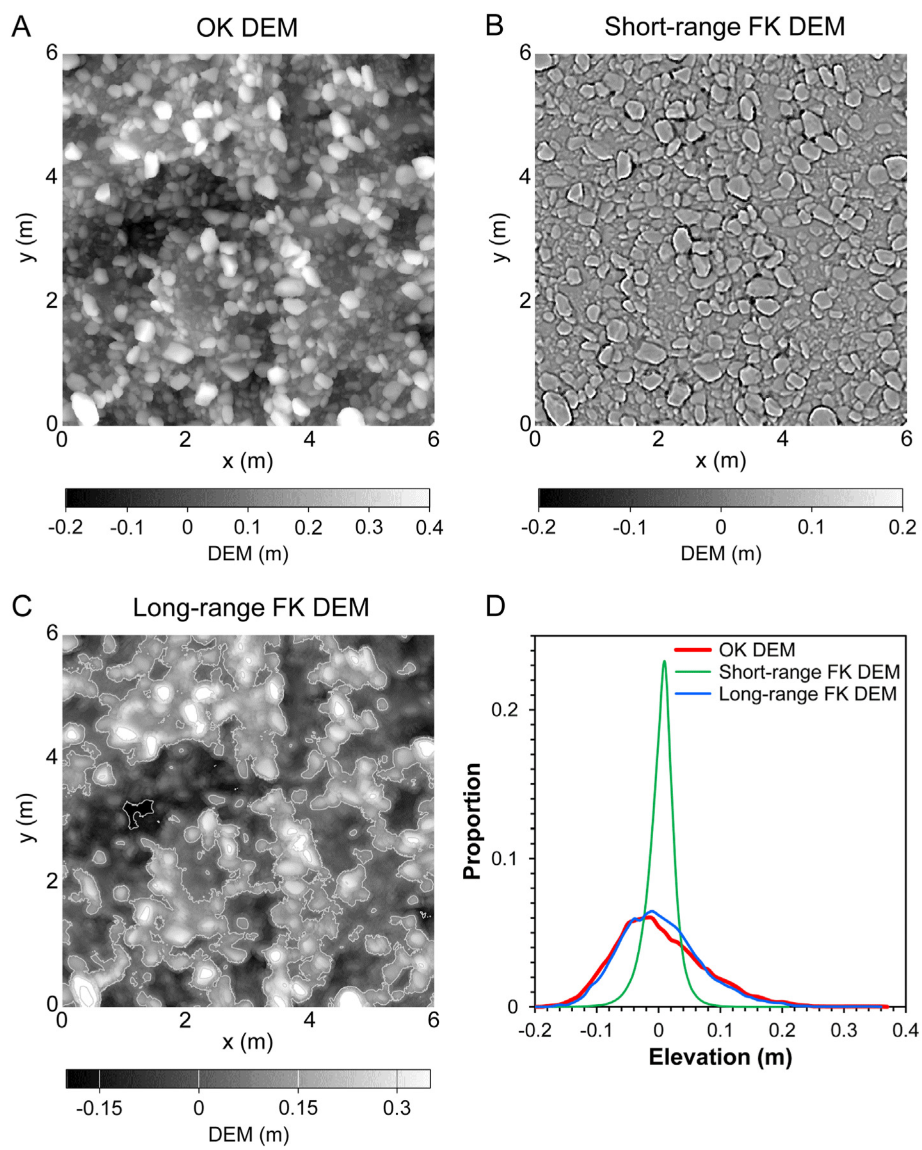

Fig. 2. An example gravel-bed patch collected from Nanshih Creek (northern Taiwan): (A) ordinary kriged (OK) DEM; (B) short-range component of factorial kriged (FK) DEM; (C) long-range component of FK DEM; (D) surface elevation distributions of OK DEM, and short- and long-range FK DEMs.

scale bedforms such as clusters. This feature recognition capability of the microform-scale DEM is used herein to devise a DEM-based approach for cluster identification. As a final note, the advantage of the FK is that the parameters used in the computations, i.e., $\gamma(h)$, $\gamma^1(h)$ and $\gamma^2(h)$, are determined directly from the variogram models without a need for trial and error. In addition, the FK DEMs are more intuitive since the full (OK) DEM is simply the sum of short- and long-range FK DEMs.

3. Case study

3.1. Study site

The study site was located at a point bar in lower Nanshih Creek near its confluence with Hsintien Creek, northern Taiwan (Fig. 3). Nanshih Creek is a mountain stream with an annual runoff of the order of 1.3 km^3. The lowest and highest monthly flows (19.6 and 84.8 m^3/s) occur, respectively, in April and September. The steep slope at the upper end of the flow duration curve (with the 1%, 5%, and 10% duration flows = 441, 128, and 79 m^3/s) indicates that these high flows are flashy responses to rainfall or typhoon events. The gravel bar remains exposed for most of the time, and is sporadically inundated and mobilized during the flood seasons in summer and fall. The exposed bar is ~100 m wide, stretching along a sharp bend ~500 m in length. A 6 m × 6 m patch of the gravel-bed surface was scanned with a terrestrial laser scanner. The size of the patch was chosen based on a prior study of this area (Huang and Wang, 2012), where a 6 m × 6 m extent was found large enough to reveal the microform-scale structures, which was also confirmed by the long range value of the empirical variogram profile (see Section 4.1). The patch was located on the bar near the outer bank where a zone of maximum bedload transport shifted from the inner bank at the upstream of the bend toward the pool (Dietrich and Smith, 1984; Clayton and Pitlick, 2007). Active transport and deposition of bedload particles gave rise to microform bed structures. The grain size distribution (GSD) was not sampled on site using Wolman-style pebble counts (Bunte and Abt, 2001), rather it was obtained using the short-range FK DEM (see Section 4.2). The median grain size D_{50} was 91 mm, the sorting coefficient σ_I was 0.83 ($=|\phi_{84}-\phi_{16}|/4+|\phi_{95}-\phi_5|/6.6$, where $\phi_i=-\log_2 D_i$), and the sorting index SI was 1.83 ($=(D_{84}/D_{50}+D_{50}/D_{16})/2$). The gravel bed was thus classified as moderately sorted (Folk and Ward, 1957; Bunte and Abt, 2001).

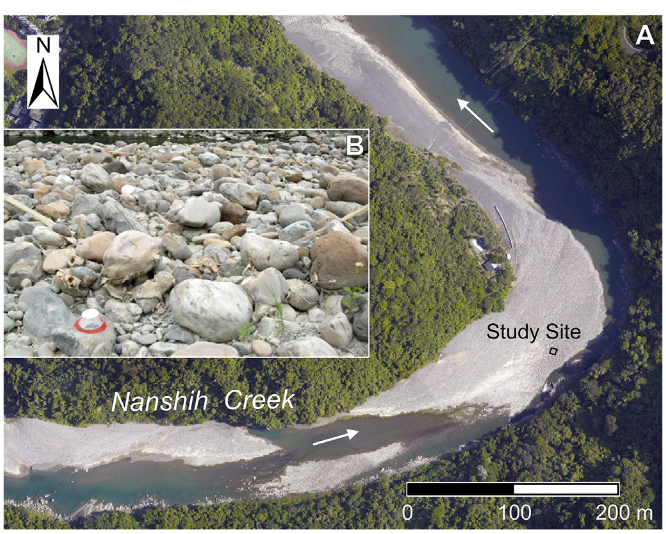

Fig. 3. (A) Orthorectified photograph of the study site (24°54′10″N, 121°33′24″E) at a point bar in lower Nanshih Creek (northern Taiwan). Scanned gravel-bed patch is indicated by a square box, flow directions are indicated by arrows. (B) Oblique view of the 6 m × 6 m gravel-bed patch, around which a 1 m wide buffer on each side was set with a yellow tape.

3.2. DEM data

The bed topography was scanned using a FARO Photon 80 terrestrial laser scanner, which has a scan range between 0.6 and 76 m and a nominal accuracy of 2 mm. Around the 6 m × 6 m gravel-bed patch, a 1 m wide buffer on each side was set with a yellow tape (Fig. 4A). Terrestrial laser scans (TLS) were performed from four directions at a distance of 8 m from the center of the patch, aimed to minimize data voids in spots hidden by large, protruding particles (Hodge et al., 2009; Wang et al., 2011). A high-resolution mode was used to generate a point spacing of 3 mm, resulting in a total of 10 million points over the patch. The TLS point cloud data were co-registered and merged by identifying the spherical targets (with high reflection contrast) placed at the corners of the patch. The density of the merged TLS data was of the order of 30 points/cm^2.

Considerable initial efforts were devoted to filtering out the "mixed pixel errors" (Hodge, 2010), which occurred near the edges of the particles where the range measurement acquired from the area of a complex surface sampled by the laser footprint was not representative of the range at the center area of that footprint. An original DEM with 1 cm × 1 cm resolution was generated with a two-stage mean-based filter (Wang et al., 2011) by identifying and averaging the TLS data points of the upmost surface. The original DEM was detrended with a planar trend surface and normalized to a zero mean. The data voids at spots hidden by protruding grains were filled via the ordinary kriging, yielding a voidless ordinary kriged (OK) DEM on 1 cm × 1 cm grids (Fig. 4B), also shown as a color hillshade map (Fig. 4C).

4. DEM-based delineation of clusters

The proposed approach consists of five steps: (1) decomposing the short- and long-range scales of the OK DEM using a nested variogram model; (2) segmenting grain boundaries using the short-range FK DEM; (3) identifying potential clusters using the long-range FK DEM; (4) delineation of individual clusters using the identified clusters and segmented grain boundaries; (5) elimination of the clusters that do not meet the specified criterion for the minimum number of constituent grains. These steps are described in the following sections.

4.1. Decomposition of short- and long-range scales

The short- and long-range spatial scales of the OK DEM were decomposed using a theoretical, nested variogram model (Fig. 5). An omni-directional empirical variogram profile was calculated over a range of lag h up to half of the DEM extent. The empirical variogram was fitted with a nested double spherical model that combines a short-range spherical model (range a_1=0.47 m, and sill $c_1=6.457\times10^{-3}$ m^2) and a long-range spherical model (range a_2= 0.962 m, and sill $c_2=4.954\times10^{-3}$ m^2). The short range a_1 represents the sediment grain scale, which corresponds to the $D_{99.5}$ of the GSD. The long range a_2 represents the microform scale. A saturation region is reached at $h>a_2$, indicating that bedforms at scales larger than ~1 m were not present in the 6 m × 6 m gravel-bed patch, which justified our choice of patch size. The short- and long-range spherical models, i.e., $\gamma^1(h)$ and $\gamma^2(h)$, were then used in Eqs. (6)–(7a) and (7b) to generate the short- and long-range FK DEMs, respectively.

4.2. Segmentation of individual grains

The short-range FK DEM (Fig. 6A) exhibits a grain-scale topographic relief. Individual grains are sharply outlined at the grain boundaries where the residual elevations exhibit a sudden transition from positive values (light gray) to negative values (dark gray). Thus, the zero-level

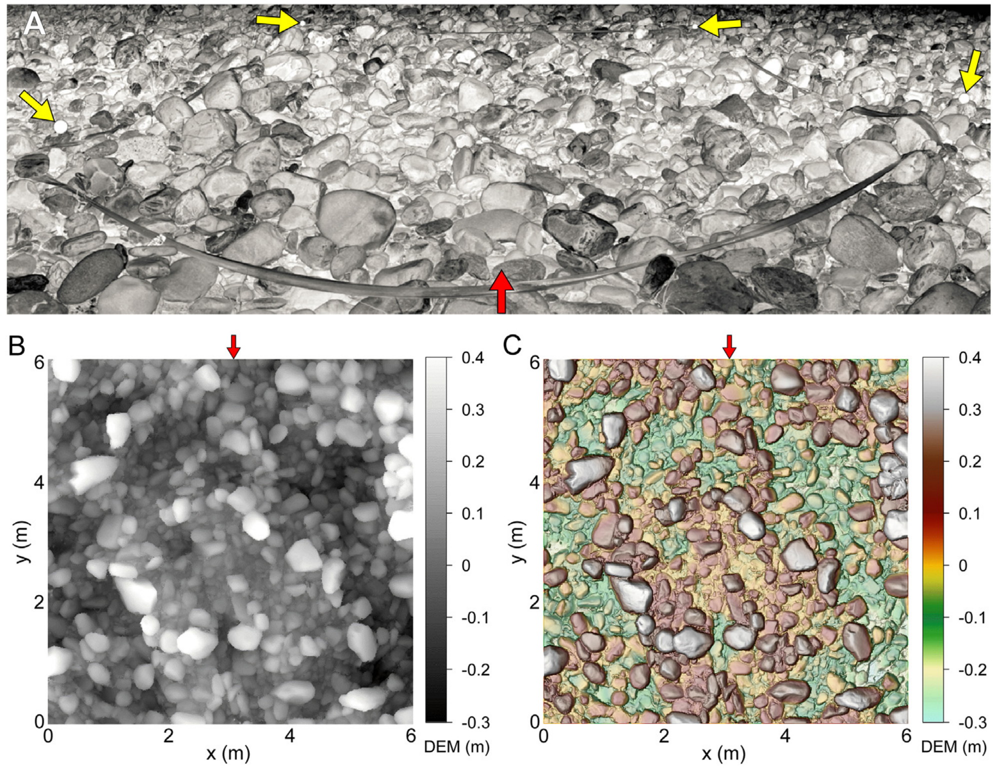

Fig. 4. (A) Oblique-perspective grayscale intensity image of terrestrial laser scanning (TLS) data. Yellow arrows point at spherical targets (14.5 cm in diameter) used for data co-registration and merge; (B) grayscale map of OK DEM (1 cm × 1 cm resolution) of the 6 m × 6 m gravel-bed patch; (C) color hillshade map of OK DEM. Red arrows point at the same location toward the same direction.

contours of the short-range FK DEM were used in this study as an aid for segmentation of grain boundaries. Fig. 6B shows the zero-level contours (white lines) of the short-range FK DEM, where individual grains

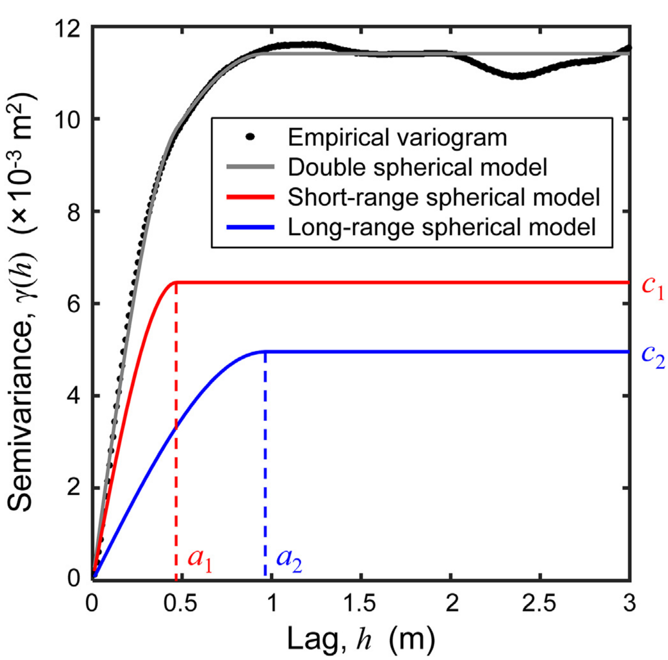

Fig. 5. Omni-directional variograms of the OK DEM: empirical variogram (solid circles) is fitted with a nested double spherical model (gray line) that combines linearly a short-range spherical model (red line) and a long-range spherical model (blue line), with the short and long ranges: a_1=0.470 m, a_2=0.962 m, and sills $c_1 = 6.457 \times 10^{-3}$ m^2, $c_2 = 4.954 \times 10^{-3}$ m^2.

(including many smaller ones) become clearly distinguishable. Some fragmentations associated with grain-surface texture are exhibited also by the zero-level contours. Such textural features on the grain surfaces, however, provide no additional information useful for grain segmentation.

Individual grains were digitized manually by a single operator in ArcGIS (Esri) on the hillshade map of OK DEM (as a base map), superimposed with the zero-level contours of the short-range FK DEM (as a visual aid). A total of 1469 grains were recognized and digitized (Fig. 6C), which were fitted with ellipses (Fig. 6D) and their *b*-axes were used to derive the GSD (Bunte and Abt, 2001), as shown in Fig. 7. The grain sizes range from 27.6 to 569.6 mm with a median size D_{50}= 91 mm. The GSD of the digitized grains is well approximated by a lognormal distribution (Fig. 7).

Although grain segmentation was done manually in this study, automation of the procedure is possible. The grain segmentation procedure of existing automated grain-sizing software, such as Digital Gravelometer (Graham et al., 2005) and BASEGRAIN (Detert and Weitbrecht, 2012, 2013), can be typically divided into three processes: (1) morphological filtering to enhance grain boundaries or interstices between grains (e.g., bottom-hat transformation); (2) detection of grain boundaries (e.g., edge detection algorithms, double-threshold approach); (3) segmentation of individual grains (e.g., dilation/skeletonization procedure, watershed segmentation). Among these processes, the second is particularly demanding given the difficulty of accurately detecting grain boundaries. Our experience with these automated grain-sizing software indicated that segmentation of individual grains with full automation remains a challenge. With the zero-level contours of the short-range FK DEM usable as a guide to delineate grain boundaries, it is possible to streamline the workflow of grain segmentation by incorporating the zero-level contours into, e.g., the algorithm of automated image segmentation recently devised by Karunatillake et al. (2014) for granulometry and sedimentology.

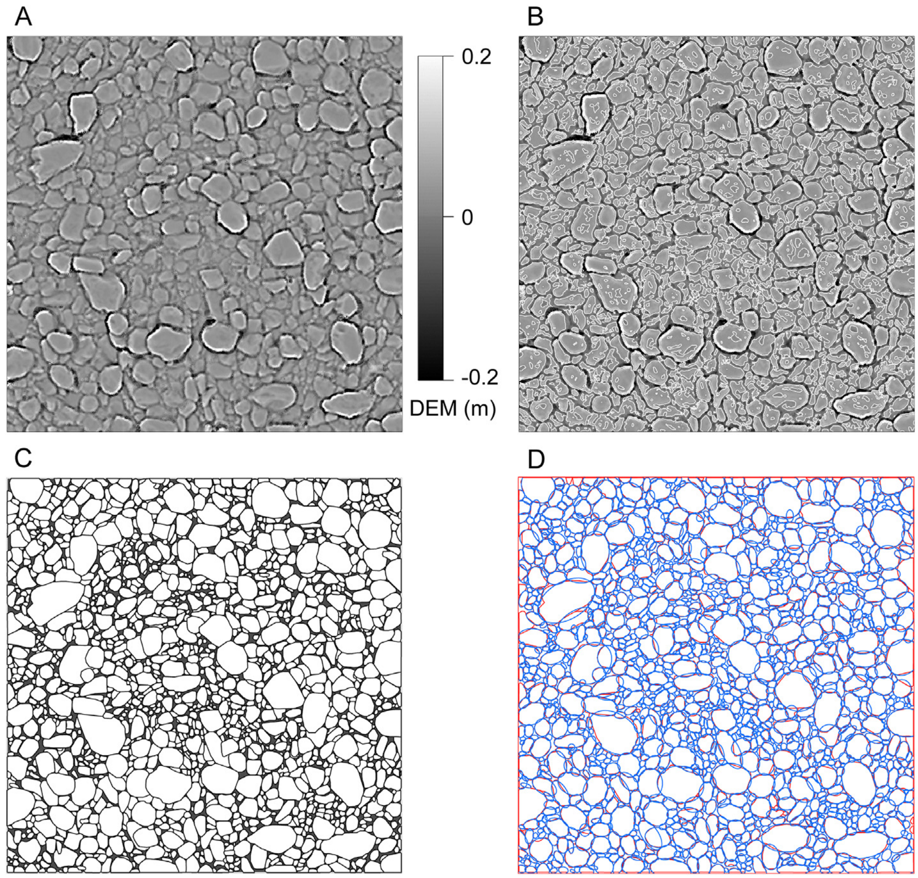

Fig. 6. (A) Grayscale map of short-range FK DEM (6 m × 6 m extent); (B) zero-level contours (white lines) superimposed on short-range FK DEM; (C) digitized grains; (D) digitized grains fitted with ellipses, whose *b*-axes were used to derive the GSD.

4.3. Identification of potential clusters

The long-range FK DEM (Fig. 8A) exhibits a topographic relief where groupings of particles emerge as microform-scale features such as clusters. The long-range FK DEM was used herein as a tool for identification of potential clusters. With the given working definition of clusters: "*discrete, organized groupings of larger particles that protrude above the local mean bed level*", a threshold elevation level was used to identify areas that "*protrude above the local mean bed level*". Shown in Fig. 8A are a set of contours ranging from the 60th to 90th percentile levels. The 90th percentile contours cover only the locally highest areas while the 60th percentile contours include more of the lower, surrounding areas. The discrete areas enclosed by a specific contour percentile level may thus correspond to individual clusters. Fig. 8B is the segmented grains superimposed on the long-range FK DEM, confirming that the identified clusters are indeed "*groupings of larger particles*". A question then arises: Which contour percentile level is suitable for delineation of clusters? This issue is addressed below.

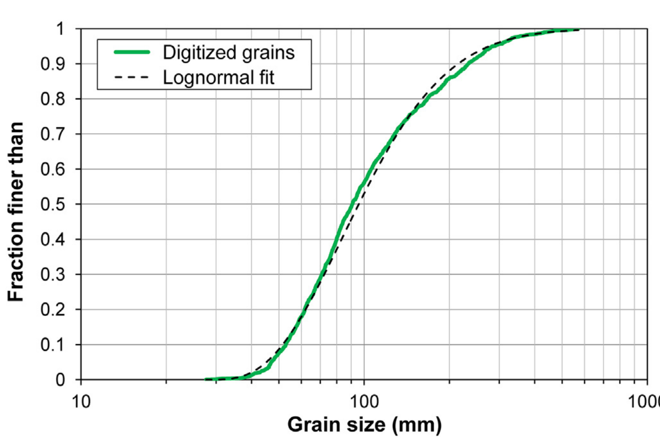

Fig. 7. Grain size distribution (GSD) derived from *b*-axes of digitized grains (Fig. 6D). The GSD is well approximated by a lognormal distribution.

4.4. Delineation of individual clusters

To illustrate how individual clusters were delineated, we show in Fig. 8C the discrete areas enclosed by the 60th percentile contours. The segmented grains were superimposed on the enclosed areas, and only those grains that overlapped fully or partially with the enclosed areas were retained. The retained particles were examined for their connectedness. Grains that were mutually connected (or in contact) were grouped into a cluster. This geoprocessing task can be done by Python scripting and automation in ArcGIS. Five clusters so delineated (numbered as 1 to 5) are shown in Fig. 8C, where the constituent grains of a cluster were filled with the same color.

In Fig. 8C, the uncolored grains that overlapped with the contour-enclosed areas but were not classified as clusters were eliminated for not meeting the specified minimum number of constituent grains. Herein, to ensure that the delineated clusters are "*organized groupings of larger grains*", we adopted a criterion: a cluster consists of at least three abutting grains. By setting the minimum number of constituent grains as three, we aimed to exclude the possibility of unorganized, random groupings. We did not specify a threshold size for anchor clast (referring to the largest grain of a cluster). However, by adopting three as the minimum number of constituent grains, the resulting

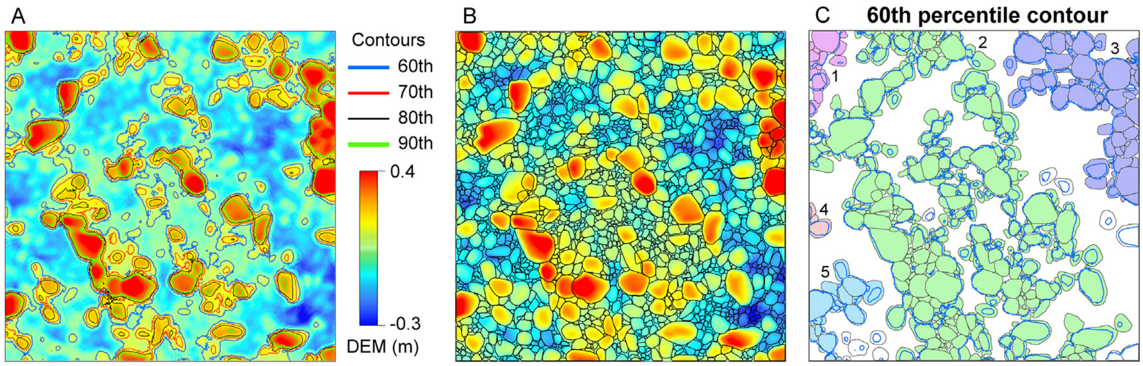

Fig. 8. (A) Color map of long-range FK DEM (6 m × 6 m extent), superimposed by contours ranging from the 60th to 90th percentile levels; (B) long-range FK DEM superimposed by digitized grains; (C) delineated clusters resulting from the 60th percentile contours (blue lines), where the constituent grains of a cluster are filled with the same color, while the uncolored grains are eliminated for not meeting the required minimum number of constituent grains. (See text for details).

anchor clasts would be consistently greater than the D_{90} of the GSD (see Section 5.1).

As shown in Fig. 8C, using the 60th percentile contours to identify and delineate potential clusters would result in oversized (or overconnected) clusters. As a result, cluster 2 alone has an area of 14.2 m^2, which is nearly 40% of the patch. The total area of these five clusters (= 19.5 m^2) exceeds 54% of the patch, far greater than the reported values, which rarely exceeded 40% (e.g., Brayshaw, 1984; Wittenberg, 2002; Wittenberg and Newson, 2005; Strom and Papanicolaou, 2008; Hendrick et al., 2010). In addition, the length and width of cluster 2 exceed the microform scale (~1 m) revealed by the variogram profile (described in Section 4.1). Clearly, the 60th percentile contours are too low to be a suitable level for delineation of clusters. In the following section, a set of contours ranging from the 70th to 90th percentile levels are used to identify and delineate clusters. The results are compared with a compilation of existing field data, their implications for practical applications are also discussed.

5. Results and discussion

5.1. Delineated clusters

Fig. 9 shows the delineated clusters resulting from the 70th to 90th percentile contours, with the statistics summarized in Table 1. With increasing contour percentile level, the number of clusters decreases monotonically from 16 to 4, and the corresponding total area of clusters also decreases from 36.6 to 9.1% of the patch (Fig. 9F). The number of constituent grains in each cluster exhibits the widest range of variation (3 to 52 grains) for the 70th percentile contour. Such range of variation reduces with increasing contour percentile level, exhibiting

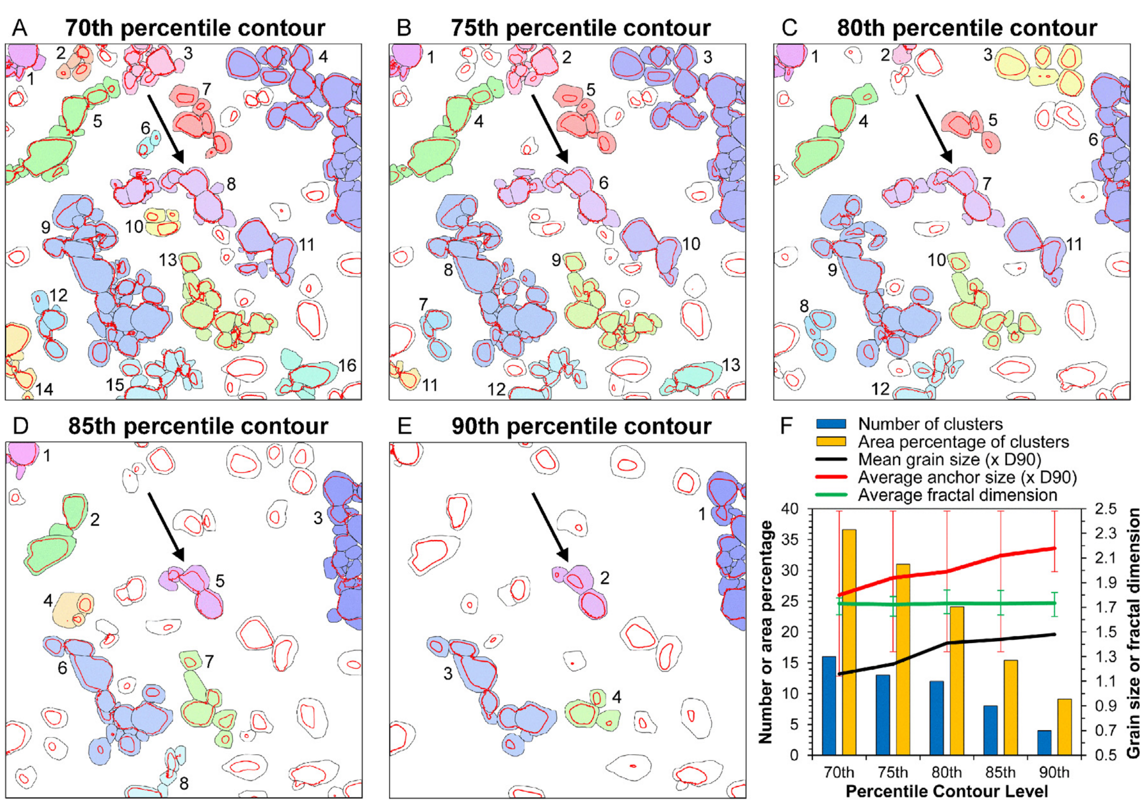

Fig. 9. Delineated clusters resulting from the (A) 70th, (B) 75th, (C) 80th, (D) 85th, and (E) 90th percentile contours of long-range FK DEM (6 m × 6 m extent), grains filled with the same colors are the constituent particles of individual clusters, uncolored grains are eliminated ones, and arrows indicate channel centerline directions; (F) summary statistics of cluster attributes.

Table 1
Attribute statistics of individual clusters delineated with the 70th to 90th percentile contours of long-range FK DEM.

Cluster ID	70th percentile contour				75th percentile contour				80th percentile contour				85th percentile contour				90th percentile contour			
	No. of grains	Area (m^2)	Anchor size ($\times D_{90}$)	D_{AT}	No. of grains	Area (m^2)	Anchor size ($\times D_{90}$)	D_{AT}	No. of grains	Area (m^2)	Anchor size ($\times D_{90}$)	D_{AT}	No. of grains	Area (m^2)	Anchor size ($\times D_{90}$)	D_{AT}	No. of grains	Area (m^2)	Anchor size ($\times D_{90}$)	D_{AT}
1	6	0.28	2.07	1.77	5	0.24	2.07	1.77	5	0.24	2.07	1.77	4	0.21	2.07	1.75	18	1.08	2.26	1.82
2	5	0.23	1.15	1.74	13	0.49	1.81	1.77	3	0.10	1.39	1.81	3	0.65	2.45	1.73	3	0.41	2.01	1.72
3	16	0.53	1.81	1.77	37	2.50	2.26	1.70	5	0.77	2.23	1.77	22	1.24	2.26	1.84	9	1.24	2.48	1.63
4	39	2.56	2.26	1.71	11	1.05	2.45	1.63	4	0.77	2.45	1.65	3	0.40	2.39	1.80	5	0.52	1.99	1.78
5	13	1.08	2.45	1.64	6	0.55	1.82	1.71	3	0.33	1.82	1.70	4	0.47	2.01	1.71				
6	3	0.10	1.14	1.75	16	0.89	2.01	1.73	24	1.26	2.26	1.84	16	1.58	2.48	1.64				
7	7	0.58	1.82	1.69	3	0.29	1.45	1.79	9	0.80	2.01	1.71	6	0.69	1.99	1.72				
8	18	0.94	2.01	1.72	44	2.58	2.48	1.70	3	0.29	1.45	1.79	5	0.30	1.34	1.67				
9	52	2.74	2.48	1.71	16	1.04	1.99	1.66	25	2.23	2.48	1.67								
10	3	0.23	1.16	1.78	4	0.55	2.39	1.71	11	0.94	1.99	1.67								
11	10	0.68	2.39	1.73	3	0.14	1.48	1.74	3	0.53	2.39	1.71								
12	5	0.39	1.45	1.75	9	0.48	1.34	1.71	7	0.41	1.34	1.70								
13	24	1.30	1.99	1.69	4	0.36	1.74	1.77												
14	7	0.38	1.48	1.76																
15	16	0.67	1.34	1.74																
16	6	0.49	1.74	1.73																
Average	14	0.82	1.80	1.73	13	0.86	1.94	1.72	9	0.72	1.99	1.73	8	0.69	2.12	1.73	9	0.81	2.18	1.74
Mean grain size of cluster ($\times D_{90}$)		1.16				1.24				1.41				1.44				1.48		
Total area (m^2)		13.18				11.17				8.67				5.55				3.26		
Area percentage		36.6				31.0				24.1				15.4				9.1		

the narrowest range (3 to 18 grains) for the 90th percentile contour. The average number of grains per cluster and average area of individual clusters, however, do not exhibit any monotonic trends with increasing contour percentile level (Table 1), varying in the ranges from 8 to 14 grains/cluster and 0.69 to 0.86 m^2/cluster.

Despite the lack of monotonic trends in the average number of grains per cluster and mean area per cluster, the mean grain size of clusters increases monotonically from 1.16 to 1.48 times the D_{90} with increasing contour percentile level (Fig. 9F). Coarsening of clusters is observable in Fig. 9A–E, where the smaller, lower grains surrounding the larger clasts are increasingly excluded with the increase of contour percentile level. Coarsening of clusters is also reflected by the average size of anchor clasts, which increases from 1.8 to 2.18 times the D_{90} with increasing contour percentile level (Fig. 9F). Variation of anchor size has the widest range for the 70th percentile contour (1.14 to 2.48 times the D_{90}) and the narrowest range for the 90th percentile contour (1.99 to 2.48 times the D_{90}). Coarsening of clusters with increasing contour percentile level indicates that a higher delineation standard tends to exclude those smaller, surrounding grains while retaining the larger and more protruding, core particles.

A striking feature of our approach is that, even though a criterion for threshold anchor size was not specified, the delineated clusters would always contain an anchor clast that is greater than the D_{90} of the GSD (Table 1). This is in contrast to the conventional approaches for cluster identification, which identify a group of abutting particles that has an anchor clast larger than the specified threshold size, and then verify the identified cluster by examining whether it protrudes above the surrounding bed surface (e.g., Oldmeadow and Church, 2006; Hendrick et al., 2010). The use of a threshold anchor size as the primary criterion for cluster identification and a bed topography as the secondary criterion is probably attributable to the fact that grain sizes are more accessible than a detailed DEM. With the support of the FK DEM, however, the delineated clusters not only protrude higher above the bed but also meet the expectation for anchor sizes. Our results thus point toward employing a DEM-based approach rather than a grain-size-based approach for cluster delineation.

Finally, the areal fractal dimension D_{AT} (Hausdorff-Besicovich dimension of the projected area) of each delineated cluster was estimated, using the box-counting approach implemented in an open source software FracLac (Karperien, 2013). The areal fractal dimension is a single aggregate index that characterizes the projected area and perimeter of a cluster, and can be used to discriminate the planform morphologies of the clusters (Papanicolaou et al., 2012). Box counting was performed to determine the number of square boxes, $N(\mu)$, of box size μ, that cover the projected area of a cluster. Given the fact that $N(\mu)$ would be negatively correlated to μ, using a series of box sizes the fractal dimension D_{AT} can be determined via the slope of the best linear fit to the $\log N(\mu)$ vs. $\log \mu$ data. To facilitate this task, each cluster was exported as a binary image and then input to FracLac. Fig. 10 shows the binary images of delineated clusters along with their D_{AT} values. In general, the D_{AT} values of individual clusters would either increase or decrease with increasing contour percentile level due to being split into smaller ones or exclusion of lower surrounding grains. However, the ranges of D_{AT} values (collectively 1.63 to 1.84) remain fairly consistent. The average values of D_{AT} with increasing contour percentile level remain nearly constant at 1.73 ± 0.01 (Table 1, Fig. 9F), indicating that clusters delineated with different contour percentile levels exhibit similar planform morphologies.

5.2. Comparison with existing field data

The results were compared with a compilation of reported field data on cluster size, density, planform morphology, and GSD information (Table 2). Clusters have been documented in a variety of settings, including: (1) headwater streams in New Zealand with different levels of flow variability and armoring, composed of metamorphic platy clasts or coarse-grained plutonic sediments (Biggs et al., 1997); (2) steep upland cobble-bed rivers and low-gradient gravel-bed rivers, and a wandering gravel-bed river in England (Wittenberg and Newson, 2005; Wittenberg et al., 2007); (3) small, perennial streams in England with well-rounded cobble beds or flint-gravel beds, and upland streams in Wales with slate gravel/cobble beds, all characterized by flashy runoff due to rainfall (Brayshaw, 1984, 1985); (4) ephemeral gravel-bed streams in Israel with relatively rare, annual flow events that follow intense rainstorms (Wittenberg, 2002; Wittenberg et al., 2007); (5) Mediterranean gravel-bed rivers in Italy characterized by deeply-incised valleys, poorly-sorted beds and flashy peak flows that occur in autumn (Brayshaw, 1985); (6) typical mountain gravel-bed rivers in USA with pool-riffle morphologies, flowing through steeply-sided glacial valleys, with runoff dominated by snowmelt or affected also by

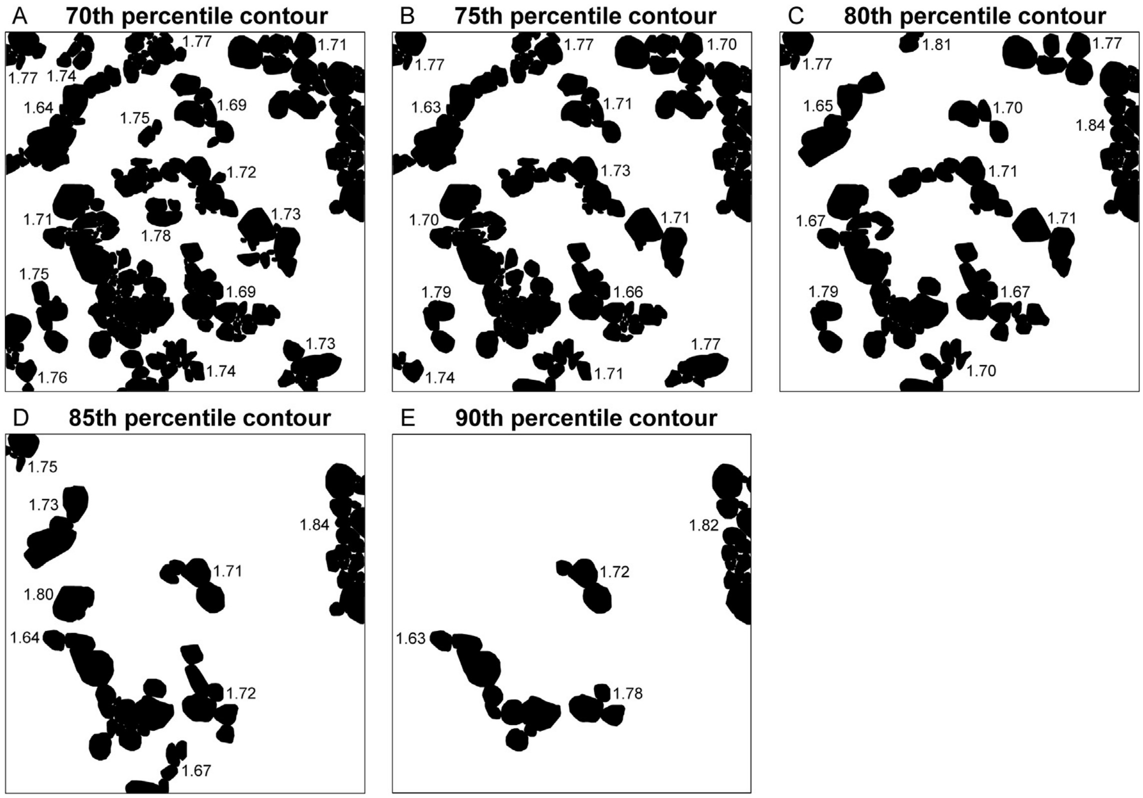

Fig. 10. Binary images of clusters delineated with the (A) 70th, (B) 75th, (C) 80th, (D) 85th, and (E) 90th percentile contours of long-range FK DEM (6 m × 6 m extent), along with the areal fractal dimension, D_{AT}, of each cluster.

Table 2
Comparison of cluster attributes from this study with those from previous field studies.

Attribute	This study	Previous field studies	Sources
Grain sizes			
D_{50} (mm)	91	30–97 (11 cobble/gravel bed rivers, NE England)	Wittenberg et al. (2007)
		40–105 (American and S.F. Snoqualmie Rivers, USA)	Strom and Papanicolaou (2008)
		29–91 (Entiat River, USA)	Hendrick et al. (2010)
D_{84} (mm)	190	45–215 (12 headwater streams, New Zealand)	Biggs et al. (1997)
		45–224 (11 cobble/gravel bed rivers, NE England)	Wittenberg et al. (2007)
		80–190 (American and S.F. Snoqualmie Rivers, USA)	Strom and Papanicolaou (2008)
		50–210 (6 cluster-dominated river beds, worldwide)	Strom and Papanicolaou (2009)
D_{90} (mm)	233	104–441 (7 rivers, NE England and Mt. Carmel Israel)	Wittenberg (2002)
		55–315 (15 rivers, NE England, Mt. Carmel/Negev Israel)	Wittenberg et al. (2007)
Sorting indices[a]			
σ_I	0.83	0.89 (East Creek, BC Canada)	Oldmeadow and Church (2006)
		0.75–1.74 (15 rivers, NE England, Mt. Carmel/Negev Israel)	Wittenberg et al. (2007)
SI	1.83	1.73 - 3.59 (7 rivers, NE England and Mt. Carmel Israel)	Wittenberg (2002)
		1.57–2.47 (dynamic equilibrium bar, River South Tyne, UK)	Wittenberg and Newson (2005)
		1.81 (East Creek, BC Canada)	Oldmeadow and Church (2006)
		1.72–3.11 (11 cobble/gravel bed rivers, NE England)	Wittenberg et al. (2007)
		<2.4 (American and S.F. Snoqualmie Rivers, USA)	Strom and Papanicolaou (2008)
Cluster density (clusters/m^2)	0.11–0.44	0.07–0.28 (12 headwater streams, New Zealand)	Biggs et al. (1997)
		0.89–1.4 (dynamic equilibrium bar, River South Tyne, UK)	Wittenberg and Newson (2005)
		0.93 (East Creek, BC Canada)	Oldmeadow and Church (2006)
		0.7–1.5 (Entiat River, USA)	Hendrick et al. (2010)
Proportion of cluster area (%)	9.1–36.6	5–10 (4 gravel-bed rivers, England and Italy)	Brayshaw (1985)
		0.7–4.4 (12 headwater streams, New Zealand)	Biggs et al. (1997)
		30–40 (4 perennial streams, NE England)	Wittenberg (2002)
		8–22 (3 ephemeral streams, Mt. Carmel Israel)	Wittenberg (2002)
		7–16 (dynamic equilibrium bar, River South Tyne, UK)	Wittenberg and Newson (2005)
		6–39 (15 rivers, NE England, Mt. Carmel/Negev Israel)	Wittenberg et al. (2007)
		3–10 (American and S.F. Snoqualmie Rivers, USA)	Strom and Papanicolaou (2008)
		>15 (cluster bars, Entiat River, USA)	Hendrick et al. (2010)
Size of anchor clast (×D_{84})	1.40–3.04	1.77–7.38 (12 headwater streams, New Zealand)	Biggs et al. (1997)
		1.11–2.72 (dynamic equilibrium bar, River South Tyne, UK)	Wittenberg and Newson (2005)
		1–1.66 (East Creek, BC Canada)	Oldmeadow and Church (2006)
		>1.18–1.85 (11 cobble/gravel bed rivers, NE England)	Wittenberg et al. (2007)
		1.22–1.95 (American and S.F. Snoqualmie Rivers, USA)	Strom and Papanicolaou (2008)
Areal fractal dimension D_{AT}	1.72–1.74	1.62–1.77 (12 clusters, American River, USA)	Papanicolaou et al. (2012)

[a] $\sigma_I = |\phi_{84} - \phi_{16}|/4 + |\phi_{95} - \phi_5|/6.6$, where $\phi_i = -\log_2 D_i$; $SI = (D_{84}/D_{50} + D_{50}/D_{16})/2$.

flash floods following rain-on-snow events or intense summer thunderstorms (Strom and Papanicolaou, 2008; Hendrick et al., 2010; Papanicolaou et al., 2012); (7) a mountain stream in a volcanic terrain in the USA, with its plane bed composed of well-sorted cobbles/pebbles and the flow regime dominated by snowmelt (de Jong, 1995); (8) an anthropogenically influenced, small headwater stream in Canada, with step-pool sequences present at the upstream side of a culvert and an armored reach developing downstream of the culvert (Oldmeadow and Church, 2006). Our results add data for a different geographic region. Further background about the settings of these reported sites can be found in the Supplementary information.

The attributes compared include grain sizes, sorting indices, cluster density, area percentage, and size of anchor clast (Table 2). Our characteristic sizes (D_{50}, D_{84}, D_{90}= 91, 190, 233 mm) are well within the grain size ranges reported, among which the sediments of the upland cobble-bed rivers in England are the coarsest whereas those of the low-gradient gravel-bed rivers in England are the finest. Our sorting indices, σ_I and SI= 0.83 and 1.83, indicating a moderately sorted river reach, resemble those of the armored East Creek in British Columbia, Canada.

Our cluster densities range from 0.11 to 0.44 clusters/m^2, which are within the reported lower bound values (headwater streams, New Zealand) and upper bound values (Entiat River, USA). The wide range of cluster densities documented in these sites is attributable to differences in flow variability, armoring and grain shape, the criteria adopted to define clusters, and the clustered bars selected for sampling (Biggs et al., 1997; Hendrick et al., 2010). Our proportions of cluster area range from 9.1 to 36.6%, which are within the lower bound values associated with the headwater streams (New Zealand) and upper bound values associated with the poorly-sorted, perennial streams (England). The sizes of anchor clasts were scaled by the D_{84} in a number of datasets compiled, with the lower bound values observed in East Creek (Canada) and upper bound values observed in headwater streams (New Zealand). As mentioned earlier, our anchor sizes range from 1.14 to 2.48 times the D_{90} (equivalent to 1.4 to 3.04 times the D_{84}), which are concordant with the reported range. In particular, our anchor sizes resemble those documented in the wandering River South Tyne (UK). Such resemblance may be attributed to their similarities in sorting indices SI and transport mechanisms. Clusters at our study site and South Tyne were both sampled from a dynamic equilibrium bar that is exposed during low flows but inundated and subjected to active transport during flashy high flow events. Flow direction at the South Tyne study site varies with the stage. Low flows run along the chute or diagonally across the bar, whereas high flows run directly downstream, normal to the chute. This is similar to the stage-dependent variation of transport direction at our study site on a point bar along a channel bend (Clayton and Pitlick, 2007).

The work of Papanicolaou et al. (2012) was the only one that documented fractal dimensions of field clusters, which included four line clusters, four triangle clusters, and four rhombic clusters recorded in a mountain gravel-bed stream (American River, USA). Their average values of D_{AT} for line, triangle, and rhombic clusters are 1.62, 1.77, and 1.76, respectively. Our average values of D_{AT}, ranging from 1.72 to 1.74, are similar to their results. The D_{AT} values of individual clusters shown in Fig. 10 also coincide with their findings, where the pseudo-line clusters on the upper left side of Fig. 10A–C exhibit the lowest values of D_{AT} (=1.64 ± 0.01), while the mega clusters on the upper right side of Fig. 10C–E (with the border cropped) exhibit the highest values of D_{AT} (=1.83 ± 0.01).

As our results fall within the ranges of reported field data, we can conclude that the FK DEM provides a novel, promising tool for cluster delineation. Currently there is no universally accepted definition of clusters, hence to recommend a standard contour percentile level for

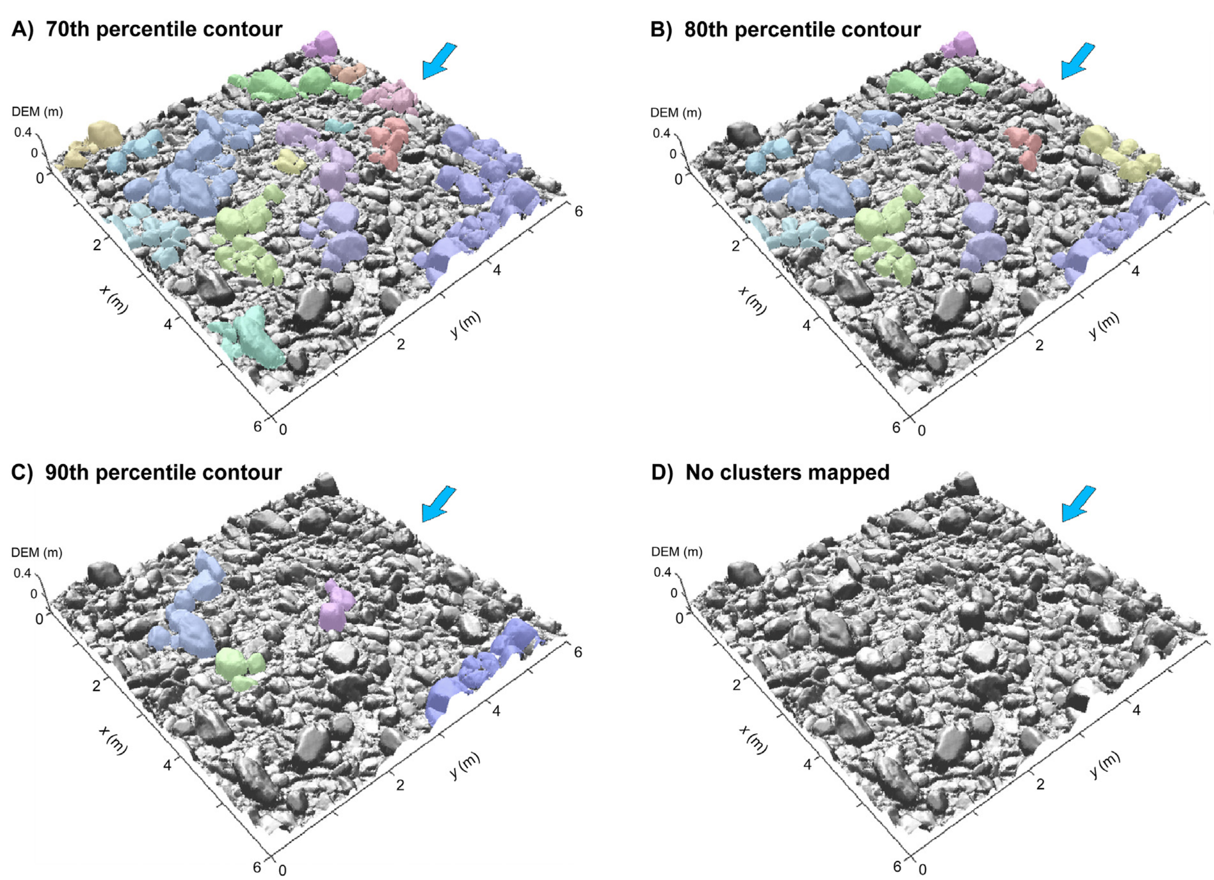

Fig. 11. 3D visualization of clusters delineated with the (A) 70th, (B) 80th, and (C) 90th percentile contours of long-range FK DEM, and (D) the same view with no clusters mapped (6 m × 6 m extent). Arrows indicate channel centerline directions.

delineation of clusters may not be practical. Nonetheless, lower levels (e.g., 70th–75th percentile contour) may be used if more of the smaller, surrounding grains are to be included. By contrast, higher levels (e.g., 80th–85th percentile contour) may be used if only those larger and more protruding, core particles are to be retained. In the absence of benchmark surfaces with correctly delineated clusters together with a unique definition for clusters, delineation of clusters will inevitably remain subjective in nature. Given that clusters vary in their constituent grains, sizes and shapes across environments, however, the parameters used in the FK, i.e., $\gamma(h)$, $\gamma^1(h)$ and $\gamma^2(h)$, can be objectively determined from the DEM-based variogram models.

Finally, it is deemed intuitive to examine the delineated clusters by 3D visualization, because it would be helpful to have a real sense of what field scientists would see on site. The color patterns of delineated clusters (Fig. 9A–E) were superimposed on the hillshade map of OK DEM in ArcScene (Esri), and exported as oblique-perspective, stereoscopic images. Fig. 11 presents the resulting images of clusters delineated with the 70th, 80th, and 90th percentile contour levels. As mentioned earlier, with increasing contour percentile level the lower, smaller grains surrounding the higher, larger clasts are increasingly excluded, leaving only the more protruding core particles. Since our approach is based on DEMs rather than grain sizes, it may exclude some of the largest but isolated clasts that are not connected or in contact with at least two sufficiently high grains to meet the definition of a cluster. These largest but isolated clasts could otherwise be classified as a cluster if the required minimum number of constituent grains is lowered as two, or a small separation distance is specified allowing for closely neighboring particles to be effectively identified as abutting ones.

6. Conclusions

In this study, we used the FK to decompose the short- and long-range (grain- and microform-scale) DEMs. The parameters used in the FK were determined from the nested variogram models derived from the OK DEM. The short-range FK DEM was used as an aid for grain segmentation. The contour percentile levels of the long-range FK DEM were used to identify potential clusters. Individual clusters were delineated on the basis of the segmented grains and identified clusters.

Our results reveal that the density and total area of delineated clusters decrease with increasing contour percentile level, while the mean grain size of clusters and average anchor size increase with the contour percentile level. These results support the observation that larger grains group as clusters and protrude higher above the bed than other smaller grains. The average areal fractal dimension of clusters shows that clusters resulting from different contour percentile levels exhibit similar planform morphologies. A striking feature of the delineated clusters is that anchor clasts are invariably greater than the D_{90} even though a threshold anchor size is not adopted herein. Comparisons with existing field data show consistency with the observed cluster attributes. Our results thus point toward a promising DEM-based approach for characterizing sediment structures in gravel-bed rivers.

Delineation of clusters is important in river science because clusters affect the flowfield near the bed, change the bed structure and are significant controls on sediment transport and thus bed stability (e.g., Robert et al., 1996; Church et al., 1998; Curran and Tan, 2014b). Essential attributes such as the spatial pattern, density, area coverage, and dimensions may be extracted from the delineated clusters. Moreover, isolating roughness scales of gravel-bed topography is increasingly applied in studies of surface processes such as armoring (Powell et al., 2016; Bertin et al., 2017). With grain boundaries segmented and clusters delineated, isolation of grain and microform DEMs could be performed on an individual grain or cluster basis, which could potentially provide further insights into the roughness parameterization.

Automation of our approach would be a direction for future efforts. With the zero-level contours of the short-range FK DEM usable as an aid to delineate grain boundaries, it is possible to streamline the workflow by integrating novel algorithms of automated grain segmentation for cluster delineation. In addition, as possible areas for improvement, omni-directional variogram may be replaced by 2D variogram surface to devise a novel, directional FK. The minimum number of constituent grains required for a cluster may be adjusted, and a small separation distance may be specified allowing for closely neighboring grains, particularly some of those largest but isolated clasts, to be effectively identified as abutting ones.

Acknowledgments

This work was supported by the Ministry of Science and Technology, Taiwan (MOST), granted to FCW (102-2221-E-002-122-MY3, 103-2221-E-002-146-MY3, and 106-2221-E-002-074-MY3). We appreciate Jordan Clayton, an anonymous reviewer, and Scott Lecce for thoughtful feedback that improved the manuscript.

Appendix A. Supplementary information

Supplementary information to this article can be found online at https://doi.org/10.1016/j.geomorph.2018.02.013.

References

Aberle, J., Nikora, V., 2006. Statistical properties of armored gravel bed surfaces. Water Resour. Res. 42. https://doi.org/10.1029/2005WR004674.

Alary, C., Demougeot-Renard, H., 2010. Factorial kriging analysis as a tool for explaining the complex spatial distribution of metals in sediments. Environ. Sci. Technol. 44: 593–599. https://doi.org/10.1021/es9022305.

Allaire, S.E., Lange, S.F., Lafond, J.A., Pelletier, B., Cambouris, A.N., Dutilleul, P., 2012. Multiscale spatial variability of CO_2 emissions and correlations with physico-chemical soil properties. Geoderma 170:251–260. https://doi.org/10.1016/j.geoderma.2011.11.019.

Atkinson, P.M., 2004. Resolution manipulation and sub-pixel mapping. In: de Jong, S.M., van der Meer, F.D. (Eds.), Remote Sensing Image Analysis: Including the Spatial Domain. Springer, pp. 51–70.

Bertin, S., Groom, J., Friedrich, H., 2017. Isolating roughness scales of gravel-bed patches. Water Resour. Res. 53:6841–6856. https://doi.org/10.1002/2016WR020205.

Biggs, B.J.F., Duncan, M.J., Francoeur, S.N., Meyer, W.D., 1997. Physical characterisation of microform bed cluster refugia in 12 headwater streams, New Zealand. N. Z. J. Mar. Freshw. Res. 31:413–422. https://doi.org/10.1080/00288330.1997.9516775.

Billi, P., 1988. A note on cluster bedform behaviour in a gravel-bed river. Catena 15: 473–481. https://doi.org/10.1016/0341-8162(88)90065-3.

Bocchi, S., Castrignanò, A., Fornaro, F., Maggiore, T., 2000. Application of factorial kriging for mapping soil variation at field scale. Eur. J. Agron. 13:295–308. https://doi.org/10.1016/S1161-0301(00)00061-7.

Bourennane, H., Hinschberger, F., Chartin, C., Salvador-Blanes, S., 2017. Spatial filtering of electrical resistivity and slope intensity: enhancement of spatial estimates of a soil property. J. Appl. Geophys. 138:210–219. https://doi.org/10.1016/j.jappgeo.2017.01.032.

Brasington, J., Vericat, D., Rychkov, I., 2012. Modeling river bed morphology, roughness, and surface sedimentology using high resolution terrestrial laser scanning. Water Resour. Res. 48. https://doi.org/10.1029/2012WR012223.

Brayshaw, A.C., 1984. Characteristics and origin of cluster bedforms in coarse-grained alluvial channels. In: Koster, E.H., Steel, R.J. (Eds.), Sedimentology of Gravels and Conglomerates, Can. Soc. Petrol. Geol, pp. 77–85.

Brayshaw, A.C., 1985. Bed microtopography and entrainment thresholds in gravel-bed rivers. Geol. Soc. Am. Bull. https://doi.org/10.1130/0016-7606(1985)96<218:BMAETI>2.0.CO.

Brayshaw, A.C., Frostick, L.E., Reid, I., 1983. The hydrodynamics of particle clusters and sediment entrapment in coarse alluvial channels. Sedimentology 30:137–143. https://doi.org/10.1111/j.1365-3091.1983.tb00656.x.

Buffin-Bélanger, T., Roy, A.G., 1998. Effects of a pebble cluster on the turbulent structure of a depth-limited flow in a gravel-bed river. Geomorphology 25:249–267. https://doi.org/10.1016/S0169-555X(98)00062-2.

Bunte, K., Abt, S.R., 2001. Sampling surface and subsurface particle-size distributions in wadable gravel- and cobble-bed streams for analysis in sediment transport, hydraulics, and streambed monitoring. General Technical Report RMRS-GTR-74. USDA Forest Service, Rocky Mountain Research Station, Fort Collins, CO (428 p.).

Butler, J.B., Lane, S.N., Chandler, J.H., 2001. Characterization of the structure of river-bed gravels using two-dimensional fractal analysis. Math. Geol. 33:301–330. https://doi.org/10.1023/a:1007686206695.

Castrignanò, A., Giugliarini, L., Risaliti, R., Martinelli, N., 2000. Study of spatial relationships among some soil physico-chemical properties of a field in central Italy using multivariate geostatistics. Geoderma 97:39–60. https://doi.org/10.1016/S0016-7061(00)00025-2.

Church, M., Hassan, M.A., Wolcott, J.F., 1998. Stabilizing self-organized structures in gravel-bed stream channels: field and experimental observations. Water Resour. Res. 34:3169–3179. https://doi.org/10.1029/98WR00484.

Clayton, J.A., Pitlick, J., 2007. Spatial and temporal variations in bed load transport intensity in a gravel bed river bend. Water Resour. Res. 43. https://doi.org/10.1029/2006WR005253.

Clifford, N.J., Robert, A., Richards, K.S., 1992. Estimation of flow resistance in gravel-bedded rivers: a physical explanation of the multiplier of roughness length. Earth Surf. Process. Landf. 17:111–126. https://doi.org/10.1002/esp.3290170202.

Cooper, J.R., Tait, S.J., 2009. Water-worked gravel beds in laboratory flumes - a natural analogue? Earth Surf. Process. Landf. 34:384–397. https://doi.org/10.1002/esp.1743.

Curran, J.C., Tan, L., 2014a. The effect of cluster morphology on the turbulent flows over an armored gravel bed surface. J. Hydro Environ. Res. 8:129–142. https://doi.org/10.1016/j.jher.2013.11.002.

Curran, J.C., Tan, L., 2014b. Effect of bed sand content on the turbulent flows associated with clusters on an armored gravel bed surface. J. Hydraul. Eng. 140:137–148. https://doi.org/10.1061/(ASCE)HY.1943-7900.0000810.

Curran, J.C., Waters, K.A., 2014. The importance of bed sediment sand content for the structure of a static armor layer in a gravel bed river. J. Geophys. Res. Earth Surf. 119:1484–1497. https://doi.org/10.1002/2014JF003143.

Detert, M., Weitbrecht, V., 2012. Automatic object detection to analyze the geometry of gravel grains – a free stand-alone tool. River Flow 2012. Taylor & Francis, London, pp. 595–600.

Detert, M., Weitbrecht, V., 2013. User guide to gravelometric image analysis by BASEGRAIN. In: Fukuoka, et al. (Eds.), Advances in River Sediment Research. Taylor & Francis, London :pp. 1789–1796. http://www.basement.ethz.ch/download/tools/basegrain.html (Jan. 2018).

Dietrich, W.E., Smith, J.D., 1984. Bed load transport in a river meander. Water Resour. Res. 20:1355–1380. https://doi.org/10.1029/WR020i010p01355.

Dobermann, A., Goovaerts, P., Neue, H.U., 1997. Scale-dependent correlations among soil properties in two tropical lowland rice fields. Soil Sci. Soc. Am. J. 61, 1483–1496.

Dubrule, O., 2003. Geostatistics for seismic data integration in earth models. Distinguished Instructor Series, No. 6. Society of Exploration Geophysicists, Tulsa, OK, USA.

Entwistle, N.S., Heritage, G.L., Johnson, K., 2008. Cluster detection and development using terrestrial laser scanning. Geophysical Research Abstracts, 10, EGU2008-A-03497. EGU General Assembly.

Folk, R.L., Ward, W.C., 1957. Brazos River bar, a study in the significance of grain size parameters. J. Sediment. Res. 27:3–26. https://doi.org/10.1306/74D70646-2B21-11D7-8648000102C1865D.

Furbish, D.J., 1987. Conditions for geometric similarity of coarse stream-bed roughness. Math. Geol. 19:291–307. https://doi.org/10.1007/BF00897840.

Galli, A., Gerdil-Neuillet, F., Dadou, C., 1984. Factorial kriging analysis: a substitute to spectral analysis of magnetic data. In: Verly, et al. (Eds.), Geostatistics for Natural Resources Characterization. Reidel, Dordrecht, Netherlands, pp. 543–557.

Goovaerts, P., 1997. Geostatistics for Natural Resources Evaluation. Oxford University Press, Oxford, UK (483 p.).

Goovaerts, P., Webster, R., 1994. Scale-dependent correlation between topsoil copper and cobalt concentrations in Scotland. Eur. J. Soil Sci. 45:79–95. https://doi.org/10.1111/j.1365-2389.1994.tb00489.x.

Goovaerts, P., Sonnet, P., Navarre, A., 1993. Factorial kriging analysis of springwater contents in the Dyle River basin, Belgium. Water Resour. Res. 29:2115–2125. https://doi.org/10.1029/93WR00588.

Goovaerts, P., Jacquez, G.M., Marcus, A., 2005a. Geostatistical and local cluster analysis of high resolution hyperspectral imagery for detection of anomalies. Remote Sens. Environ. 95:351–367. https://doi.org/10.1016/j.rse.2004.12.021.

Goovaerts, P., Jacquez, G.M., Greiling, D., 2005b. Exploring scale-dependent correlations between cancer mortality rates using factorial kriging and population-weighted semivariograms. Geogr. Anal. 37:152–182. https://doi.org/10.1111/j.1538-4632.2005.00634.x.

Graham, D.J., Reid, I., Rice, S.P., 2005. Automated sizing of coarse-grained sediments: image-processing procedures. Math. Geol. 37:1–28. http://www.sedimetrics.com (Jan. 2018).

Hardy, R.J., Best, J.L., Lane, S.N., Carbonneau, P.E., 2009. Coherent flow structures in a depth-limited flow over a gravel surface: the role of near-bed turbulence and influence of Reynolds number. J. Geophys. Res. Earth Surf. 114. https://doi.org/10.1029/2007JF000970.

Hassan, M.A., Church, M., 2000. Experiments on surface structure and partial sediment transport on a gravel bed. Water Resour. Res. 36:1885–1895. https://doi.org/10.1029/2000WR900055.

Hassan, M.A., Reid, I., 1990. The influence of microform bed roughness elements on flow and sediment transport in gravel bed rivers. Earth Surf. Process. Landf. 15, 739–750.

Hassan, M.A., Smith, B.J., Hogan, D.L., Luzi, D.S., Zimmermann, A.E., Eaton, B.C., 2008. Sediment storage and transport in coarse bed streams: scale considerations. In: Habersack, et al. (Eds.), Gravel-Bed Rivers VI: From Process Understanding to River Restoration. Elsevier, Amsterdam, Netherland, pp. 473–496.

Heays, K.G., Friedrich, H., Melville, B.W., 2014. Laboratory study of gravel-bed cluster formation and disintegration. Water Resour. Res. 50:2227–2241. https://doi.org/10.1002/2013WR014208.

Hendrick, R.R., Ely, L.L., Papanicolaou, A.N., 2010. The role of hydrologic processes and geomorphology on the morphology and evolution of sediment clusters in gravel-bed rivers. Geomorphology 114:483–496. https://doi.org/10.1016/j.geomorph.2009.07.018.

Hodge, R.A., 2010. Using simulated terrestrial laser scanning to analyse errors in high-resolution scan data of irregular surfaces. ISPRS J. Photogramm. Remote Sens. 65: 227–240. https://doi.org/10.1016/j.isprsjprs.2010.01.001.

Hodge, R., Brasington, J., Richards, K., 2009. Analysing laser-scanned digital terrain models of gravel bed surfaces: linking morphology to sediment transport processes and hydraulics. Sedimentology 56:2024–2043. https://doi.org/10.1111/j.1365-3091.2009.01068.x.

Huang, G.H., Wang, C.K., 2012. Multiscale geostatistical estimation of gravel-bed roughness from terrestrial and airborne laser scanning. IEEE Geosci. Remote Sens. Lett. 9: 1084–1088. https://doi.org/10.1109/LGRS.2012.2189351.

Isaaks, E.H., Srivastava, R.M., 1989. An Introduction to Applied Geostatistics. Oxford University Press, New York (561 p.).

Jaquet, O., 1989. Factorial kriging analysis applied to geological data from petroleum exploration. Math. Geol. 21:683–691. https://doi.org/10.1007/BF00893316.

de Jong, C., 1995. Temporal and spatial interactions between river bed roughness, geometry, bedload transport and flow hydraulics in mountain streams – examples from Squaw Creek, Montana (USA) and Schmiedlaine/Lainbach (Upper Germany). Berl. Geowiss. Abh. 59, 229.

de Jong, C., Ergenzinger, P., 1995. The interrelations between mountain valley form and river-bed arrangement. In: Hickin (Ed.), River Geomorphology. Wiley, Chichester, pp. 55–91.

Journel, A.G., Huijbregts, C.J., 1978. Mining Geostatistics. Academic Press, London (600 p.).

Karperien, A., 2013. FracLac for ImageJ. http://rsb.info.nih.gov/ij/plugins/fraclac/FLHelp/Introduction.htm, Accessed date: January 2018.

Karunatillake, S., McLennan, S.M., Herkenhoff, K.E., Husch, J.M., Hardgrove, C., Skok, J.R., 2014. A martian case study of segmenting images automatically for granulometry and sedimentology, part 1: algorithm. Icarus 229:400–407. https://doi.org/10.1016/j.icarus.2013.10.001.

Kerry, R., Goovaerts, P., Haining, R.P., Ceccato, V., 2010. Applying geostatistical analysis to crime data: car-related thefts in the Baltic states. Geogr. Anal. 42:53–77. https://doi.org/10.1111/j.1538-4632.2010.00782.x.

Lacey, R.W.J., Roy, A.G., 2007. A comparative study of the turbulent flow field with and without a pebble cluster in a gravel bed river. Water Resour. Res. 43. https://doi.org/10.1029/2006WR005027.

L'Amoreaux, P., Gibson, S., 2013. Quantifying the scale of gravel-bed clusters with spatial statistics. Geomorphology 197:56–63. https://doi.org/10.1016/j.geomorph.2013.05.002.

Lawless, M., Robert, A., 2001a. Three-dimensional flow structure around small-scale bedforms in simulated gravel-bed environment. Earth Surf. Process. Landf. 26: 507–522. https://doi.org/10.1002/esp.195.

Lawless, M., Robert, A., 2001b. Scales of boundary resistance in coarse-grained channels: turbulent velocity profiles and implications. Geomorphology 39:221–238. https://doi.org/10.1016/S0169-555X(01)00029-0.

Lv, J., Liu, Y., Zhang, Z., Dai, J., 2013. Factorial kriging and stepwise regression approach to identify environmental factors influencing spatial multi-scale variability of heavy metals in soils. J. Hazard. Mater. 261:387–397. https://doi.org/10.1016/j.jhazmat.2013.07.065.

Ma, Y.Z., Royer, J.J., Wang, H., Wang, Y., Zhang, T., 2014. Factorial kriging for multiscale modelling. J. South. Afr. Inst. Min. Metall. 114, 651–657.

Mao, L., 2012. The effect of hydrographs on bed load transport and bed sediment spatial arrangement. J. Geophys. Res. Earth Surf. 117. https://doi.org/10.1029/2012JF002428.

Mao, L., Cooper, J.R., Frostick, L.E., 2011. Grain size and topographical differences between static and mobile armour layers. Earth Surf. Process. Landf. 36:1321–1334. https://doi.org/10.1002/esp.2156.

Marion, A., Tait, S.J., McEwan, I.K., 2003. Analysis of small-scale gravel bed topography during armoring. Water Resour. Res. 39. https://doi.org/10.1029/2003WR002367.

Matheron, G., 1971. The theory of regionalized variables and its applications. Cahiers du Centre de Morphologie Mathématique, s. 1. Fontainebleau, France.

Matheron, G., 1982. Pour une Analyse Krigeante de Données Régionalisées: Note interne, N-732. Centre de Géostatistique, Fontainebleau, France (22 p.).

Milan, D., Heritage, G., 2012. LiDAR and ADCP use in gravel-bed rivers: advances since GBR6. In: Church, et al. (Eds.), Gravel-Bed Rivers: Processes, Tools, Environments. Wiley, Chichester, UK, pp. 286–302.

Nikora, V.I., Goring, D.G., Biggs, B.J.F., 1998. On gravel-bed roughness characterization. Water Resour. Res. 34:517–527. https://doi.org/10.1029/97WR02886.

Oldmeadow, D.F., Church, M., 2006. A field experiment on streambed stabilization by gravel structures. Geomorphology 78:335–350. https://doi.org/10.1016/j.geomorph.2006.02.002.

Oliver, M.A., Webster, R., 1986. Semi-variograms for modelling the spatial pattern of landform and soil properties. Earth Surf. Process. Landf. 11:491–504. https://doi.org/10.1002/esp.3290110504.

Oliver, M.A., Webster, R., Slocum, K., 2000. Filtering SPOT imagery by kriging analysis. Int. J. Remote Sens. 21:735–752. https://doi.org/10.1080/014311600210542.

Paola, C., Seal, R., 1995. Grain size patchiness as a cause of selective deposition and downstream fining. Water Resour. Res. 31, 1395–1407.

Papanicolaou, A.N., Strom, K., Schuyler, A., Talebbeydokhti, N., 2003. The role of sediment specific gravity and availability on cluster evolution. Earth Surf. Process. Landf. 28: 69–86. https://doi.org/10.1002/esp.427.

Papanicolaou, A.N.T., Tsakiris, A.G., Strom, K.B., 2012. The use of fractals to quantify the morphology of cluster microforms. Geomorphology 139–140:91–108. https://doi.org/10.1016/j.geomorph.2011.10.007.

Pebesma, E.J., 2004. Multivariable geostatistics in S: the gstat package. Comput. Geosci. 30:683–691. https://cran.r-project.org/package=gstat (Jan. 2018).

Piedra, M.M., Haynes, H., Hoey, T.B., 2012. The spatial distribution of coarse surface grains and the stability of gravel river beds. Sedimentology 59:1014–1029. https://doi.org/10.1111/j.1365-3091.2011.01290.x.

Powell, D.M., Ockelford, A., Rice, S.P., Hillier, J.K., Nguyen, T., Reid, I., Tate, N.J., Ackerley, D., 2016. Structural properties of mobile armors formed at different flow strengths in gravel-bed rivers. J. Geophys. Res. Earth Surf. 121:1494–1515. https://doi.org/10.1002/2015JF003794.

Reid, I., Frostick, L.E., Brayshaw, A.C., 1992. Microform roughness elements and the selective entrainment and entrapment of particles in gravel-bed rivers. In: Billi, et al. (Eds.), Dynamics of Gravel-Bed Rivers. Wiley, Chichester, pp. 253–276.

Reis, A.P., Sousa, A.J., Ferreira Da Silva, E., Patinha, C., Fonseca, E.C., 2004. Combining multiple correspondence analysis with factorial kriging analysis for geochemical mapping of the gold-silver deposit at Marrancos (Portugal). Appl. Geochem. 19: 623–631. https://doi.org/10.1016/j.apgeochem.2003.09.003.

Rice, S.P., Buffin-Bélanger, T., Reid, I., 2014. Sensitivity of interfacial hydraulics to the microtopographic roughness of water-lain gravels. Earth Surf. Process. Landf. 39: 184–199. https://doi.org/10.1002/esp.3438.

Robert, A., 1988. Statistical properties of sediment bed profiles in alluvial channels. Math. Geol. 20:205–225. https://doi.org/10.1007/BF00890254.

Robert, A., 1991. Fractal properties of simulated bed profiles in coarse-grained channels. Math. Geol. 23:367–382. https://doi.org/10.1007/BF02065788.

Robert, A., Roy, A.G., DeSerres, B., 1996. Turbulence at a roughness transition in a depth limited flow over a gravel bed. Geomorphology 16:175–187. https://doi.org/10.1016/0169-555X(95)00143-S.

Sandjivy, L., 1984. The factorial kriging analysis of regionalized data: its application to geochemical prospecting. In: Verly, et al. (Eds.), Geostatistics for Natural Resources Characterization. Reidel, Dordrecht, Netherlands, pp. 559–571.

Smart, G.M., Duncan, M.J., Walsh, J.M., 2002. Relatively rough flow resistance equations. J. Hydraul. Eng. 128:568–578. https://doi.org/10.1061/(ASCE)0733-9429(2002)128:6(568).

Strom, K.B., Papanicolaou, A.N., 2008. Morphological characterization of cluster microforms. Sedimentology 55:137–153. https://doi.org/10.1111/j.1365-3091.2007.00895.x.

Strom, K.B., Papanicolaou, A.N., 2009. Occurrence of cluster microforms in mountain rivers. Earth Surf. Process. Landf. 34:88–98. https://doi.org/10.1002/esp.1693.

Strom, K., Papanicolaou, A.N., Evangelopoulos, N., Odeh, M., 2004. Microforms in gravel bed rivers: formation, disintegration, and effects on bedload transport. J. Hydraul. Eng. 130:554–567. https://doi.org/10.1061/(ASCE)0733-9429(2004)130:6(554).

Strom, K.B., Papanicolaou, A.N., Constantinescu, G., 2007. Flow heterogeneity over 3D cluster microform: laboratory and numerical investigation. J. Hydraul. Eng. 133: 273–287. https://doi.org/10.1061/(ASCE)0733-9429(2007)133:3(273).

Van Meirvenne, M., Goovaerts, P., 2002. Accounting for spatial dependence in the processing of multi-temporal SAR images using factorial kriging. Int. J. Remote Sens. 23: 371–387. https://doi.org/10.1080/01431160010014800.

Wang, C.K., Wu, F.C., Huang, G.H., Lee, C.Y., 2011. Mesoscale terrestrial laser scanning of fluvial gravel surfaces. IEEE Geosci. Remote Sens. Lett. 8:1075–1079. https://doi.org/10.1109/LGRS.2011.2156758.

Webster, R., Oliver, M.A., 2007. Geostatistics for Environmental Scientists. 2nd ed. Wiley, Chichester (330 p.).

Wen, R., Sinding-Larsen, R., 1997. Image filtering by factorial kriging—sensitivity analysis and application to Gloria side-scan sonar images. Math. Geol. 29:433–468. https://doi.org/10.1007/BF02775083.

Wittenberg, L., 2002. Structural patterns in coarse gravel river beds: typology, survey and assessment of the roles of grain size and river regime. Geogr. Ann. Ser. A-Physical Geogr. 84A:25–37. https://doi.org/10.1111/j.0435-3676.2002.00159.x.

Wittenberg, L., Newson, M.D., 2005. Particle clusters in gravel-bed rivers: an experimental morphological approach to bed material transport and stability concepts. Earth Surf. Process. Landf. 30:1351–1368. https://doi.org/10.1002/esp.1184.

Wittenberg, L., Laronne, J.B., Newson, M.D., 2007. Bed clusters in humid perennial and Mediterranean ephemeral gravel-bed streams: the effect of clast size and bed material sorting. J. Hydrol. 334:312–318. https://doi.org/10.1016/j.jhydrol.2006.09.028.

Yao, T., Mukerji, T., Journel, A.G., Mavko, G., 1999. Scale matching with factorial kriging for improved porosity estimation from seismic data. Math. Geol. 31:23–46. https://doi.org/10.1023/A:1007589213368.